machines

MDPI

Article

Study on the Customization of Robotic Arms for Spray-Coating Production Lines

Chao-Chung Liu [1,*], Jun-Chi Liu [2] and Chao-Shu Liu [3]

[1] School of Computer Science and Software, Zhaoqing University, Zhaoqing 526061, China
[2] Department of Industrial Design, National United University, Miaoli 360301, Taiwan
[3] Department of Mechanical Engineering, National Kaohsiung University of Science and Technology, Kaohsiung 80778, Taiwan; joshualiu@nkust.edu.tw
* Correspondence: liuzhaozhong@zqu.edu.cn

Abstract: This paper focuses on the design and development of a customized 7-axis suspended robotic arm for automated spraying production lines. The design process considers factors such as workspace dimensions, workpiece sizes, and suspension positions. After analyzing degrees of freedom and workspace coordinates, 3D modeling ensures the arm can reach designated positions and orientations. Servo motors and reducers are selected based on load capacity and speed requirements. A suspended body method allows flexible use within the workspace. Kinematics analysis is conducted, followed by trajectory-tracking experiments using the manifold deformation control method. Results from simulation and real experiments show minimal error in tracking, demonstrating the effectiveness of the control method. Finally, the actual coating thickness sprayed by the 7-axis suspended robotic arm at four locations on the motorcycle shell was measured. The results show that the measured values at each location fall within the standard range provided by the manufacturer, demonstrating consistency in spraying across different regions. This consistency highlights the precision and effectiveness of the robotic arm's control system in achieving uniform coating thickness, even on complex and curved surfaces. Therefore, the robotic arm has been successfully applied in a factory's automated spraying production line.

Keywords: customized; suspended; 7-axis; tracking control

Academic Editor: Dan Zhang

Received: 1 December 2024
Revised: 29 December 2024
Accepted: 30 December 2024
Published: 31 December 2024

Citation: Liu, C.-C.; Liu, J.-C.; Liu, C.-S. Study on the Customization of Robotic Arms for Spray-Coating Production Lines. *Machines* **2025**, *13*, 23. https://doi.org/10.3390/machines13010023

1. Introduction

With advancements in robot manufacturing and operational technology, various types of robots have wholly integrated into our daily lives, providing diverse services and assistance across different fields. Especially, robotic arms, known for their flexibility, robustness, and precision, are widely used on today's automated production lines in factories. Given the differing environments and requirements of various production lines, the design and development of customized robotic arms have become an important area of research [1–5].

Robotic arms on production lines typically have various kinds of configurations such as 5-axis, 6-axis, and 7-axis types. For a 5-axis robotic arm, due to insufficient degrees of freedom (DOF), there are unreachable positions and orientations within the workspace. This makes controlling a given orientation and trajectory relatively challenging. In the research of 5-axis robotic arm, Chiaverini and Villani [6] provided insights into interaction control schemes that helped 5-DOF manipulators achieve desired trajectories despite their DOF limitations. Xu et al. [7] focused on inverse kinematics for 5-DOF arms, detailing

methods for solving reachability issues within a constrained workspace and limited degrees of freedom. Manjaree et al. [8] provided a comprehensive comparison of kinematic methods for a 5-DOF industrial robot, focusing on both forward and inverse kinematics. The study examined traditional Denavit–Hartenberg (DH) parameterization with advanced numerical methods for solving inverse kinematics, evaluating each approach's computational efficiency, accuracy, and suitability for industrial applications. Chen et al. [9] presented the kinematic analysis and application of a 5-degree-of-freedom robotic manipulator featuring a special joint. The results highlighted the unique kinematic characteristics introduced by this joint and its impact on the manipulator's performance. Zhong et al. [10] used a kinematic analysis and trajectory planning approach for a continuum manipulator. From these results, the non-linear behavior of the manipulator is solved through advanced algorithms to optimize its performance in complex tasks. Wen et al. [11] employed a model-predictive control algorithm to predict future robot states and adjust control actions in real-time, optimizing both position and force outputs. By integrating force and position control, the robot effectively handled tasks with varying dynamics, such as precise assembly or manipulation under uncertain conditions.

In contrast, a 6-axis robotic arm offers greater flexibility and can reach any specified pose within its working space, allowing for precise control of both position and orientation. This capability is essential for tasks like complex assembly or welding. However, when obstacles along the motion path block movement or when the end effector reaches a singularity, smooth motion and accurate positioning are affected. These issues emphasize the importance of advanced motion planning and trajectory optimization to ensure reliable performance, even in complex environments. Lattanzi et al. [12] developed a calibration procedure to correct geometric errors caused by factors such as manufacturing imperfections, joint wear, and misalignments, ensuring the robot achieves high accuracy in critical applications. Chen and Chang [13] demonstrated that a 6-axis robotic arm, enhanced with advanced vision algorithms, could autonomously detect and classify objects during inspection, significantly improving the speed and accuracy of quality control processes. The experimental results showed that the system achieves high precision in both object detection and recognition. Cheng et al. [14] identified singularity conditions and proposed methods to resolve them, such as adjusting trajectory planning and implementing kinematic control techniques to prevent the robot from reaching singular positions. In their study, these methods, through simulations, enhanced the manipulator's performance and expanded its operational range. Kim et al. [15] analyzed singularities in 6-DOF manipulators using an analytical representation of the determinant. By representing the determinant of the Jacobian matrix analytically, the paper provided a systematic and computationally efficient approach to singularity detection. Li et al. [16] introduced an optimal singularity-free motion planning method for a 6-DOF parallel manipulator. The paper focused on optimizing the motion trajectory to avoid singular configurations, ensuring smooth and controllable operation. Zhang et al. [17] analyzed the singular configurations of robotic manipulators, identifying the conditions that lead to singularities. The study provided a comprehensive theoretical framework for characterizing and predicting these singularities, which was crucial for effective motion planning and control in robotic systems. Jin et al. [18] designed a 6-DOF parallel manipulator that decoupled translation and rotation, allowing for independent control of each motion. By separating translational and rotational movements, the manipulator achieves improved performance in tasks requiring high precision. Liu et al. [19] proposed a practical solution for real-time motion planning, enabling the robot to dynamically adjust its trajectory to avoid singularities, ensuring smoother and more controlled motion. This approach was especially valuable for industrial applications, such as assembly, welding, and material handling. Gao et al. [20] introduced

a systematic approach that combined optimization algorithms and experimental data to refine the robot's model, reducing errors and improving overall performance in structural parameter identification for 6-DOF industrial robots. Djuric et al. [21] provided methods for detecting and avoiding singularities, ensuring better performance and reliability in reconfigurable manufacturing systems. By understanding these singular configurations, the research contributed to improving the efficiency, flexibility, and precision of robotic systems. Filiposka et al. [22] conducted a complexity analysis of methods for calculating the Jacobian matrix in 6-DOF reconfigurable robotic systems. Their study explored the relationship between joint velocities and end-effector movement by evaluating various approaches for efficient Jacobian computation. Reboucas et al. [23] proposed a genetic algorithm approach for tracking trajectories near singularities in robotic manipulators. This method optimized motion planning to maintain smooth and stable movement, even when passing through singular configurations.

In comparison, the human arm is much more complex, primarily due to its seven degrees of freedom, which enable it to perform more complex movements. For instance, in confined spaces where intricate motions are required, a 7-axis robotic arm can successfully execute tasks such as surface welding. This type of robotic arm, often referred to as a redundant degree-of-freedom arm, offers enhanced flexibility. The extra axis allows the arm to avoid specific interference points and enables the end effector to reach designated positions more easily. However, in motion planning for redundant robotic arms, if constraint conditions are not set, the numerical solution process for inverse kinematics can lead to indeterminate solutions for each control axis, resulting in computational difficulties. To solve this issue, the most widely applied method, whether in closed-form or iterative approaches, is velocity solving using the Jacobian matrix. In much of the literature on 7-axis robotic arms, Kuhlemann et al. [24] illustrated the advantages and key aspects of robotic systems with seven degrees of freedom. Simulation results showed that adding a seventh joint increased the manipulator's average dexterity by 16.8%. Huang et al. [25] employed a systematic approach that integrated analytical and numerical techniques to efficiently solve the inverse kinematics problem for 7-degree-of-freedom manipulators. This solution enhanced the precision and flexibility of robotic systems in performing complex tasks. Atawnih et al. [26] introduced a kinematic control approach specifically designed for redundant robots, including those with more than 6 degrees of freedom. Experimental results demonstrated that this method effectively avoided joint limit violations while maintaining smooth and precise control of the end effector's position and orientation. Asfour and Dillmann [27] showed that the closed-form kinematic solution contributed to the robot's ability to achieve dexterous and coordinated arm movements, which were important for applications in service robotics, human–robot interaction, and assistive technology. Shimizu et al. [28] presented an analytical solution for the inverse kinematics of 7-degree-of-freedom redundant manipulators, solving the key point posed by joint limits. This method enabled the precise calculation of joint angles while avoiding joint limit violations for achieving effective redundancy resolution in complex tasks. Yan et al. [29] introduced an analytical method for solving the inverse kinematics of redundant manipulators using dual arm-angle parameterization. This approach efficiently calculated joint configurations for manipulators with additional degrees of freedom, improving flexibility in achieving precise positioning and orientation. Oh et al. [30] proposed an analytical inverse kinematics solution for a 7-DOF manipulator that accounted for joint constraints and self-collision avoidance. Simulation results enabled precise calculation of joint angles to reach target end-effector positions, while ensuring safe operation within joint limits and preventing self-collisions. Chen et al. [31] examined the kinematics and singularity issues of 7-DOF redundant manipulators featuring elbow joint offsets. They also provided a detailed

analysis of singularity configurations specific to this manipulator design and offered ways to avoid these positions, enhancing reliability and precision. Hollerbach [32] focused on optimizing the kinematic design of a 7-DOF manipulator to enhance its performance in complex environments. This study tried to maximize the manipulator's reach, dexterity, and control while minimizing the probability of encountering singularities. Li and Han [33] presented an approach for solving the inverse kinematics of a 7-DOF robotic arm using a space vector method. This method simplified the computation of solving the complexities associated with redundant degrees of freedom, by improving computational efficiency and accuracy. Li and Hofbaur [34] analyzed identifying and characterizing singular configurations that reduced controllability and motion precision in a 7-DOF serial redundant manipulator. Their study provided a systematic approach for detecting these singularities to avoid positions of the manipulator to reduce degrees of freedom and effective control. Chou and Liu [35] presented an analytical solution for the inverse kinematics of 7-DOF anthropomorphic manipulators, solving joint limit constraints and singularity problems. This method, through simulation, enabled precise calculation of joint angles while avoiding problematic configurations.

Robotic arms have been typically installed in one of three main configurations: floor-mounted, wall-mounted, or ceiling-suspended [36–39]. Subir [36] and Wilson [37] demonstrated that suspending parts of a robotic arm from the ceiling not only conserved valuable floor space but also reduced obstructions, enabling streamlined movement in crowded environments. This arrangement was particularly advantageous in industries where cleanliness and space efficiency were crucial, such as pharmaceuticals and electronics. Kabra et al. [38] and Olivares-Mendez et al. [39] emphasized that suspended robotic arms extend the robot's reach, enhancing its range for tasks like packaging and assembly. By eliminating floor space constraints, these robots could access multiple workstations or conveyors with fewer spatial limitations, making them ideal for large-scale or high-throughput environments.

In summary, this study aims to design and develop a customized 7-axis suspended robotic arm for automated spraying production lines, satisfying the requirements for flexible operation within the workspace and solving diverse spray-coating needs for various workpieces. Considering factors such as workspace, arm weight, load capacity, and movement speed, a 7-axis suspended robotic arm has been comprehensively designed and constructed. To enhance motion control, an arm angle parameterization method is employed for redundancy resolution, allowing real-time tracking of each joint's precise angle and position. This setup enables effective path planning techniques that allow the robotic arm to generate and adjust optimal motion paths to avoid collisions and maintain smoothness and accuracy in the spray-coating trajectory. The motion control system integrates a multi-axis servo control core with an embedded manifold deformation controller, enabling highly responsive operation and efficient handling of complex path planning. Through this system, the robotic arm can flexibly obtain multi-axis motion demands and perform dynamic trajectory adjustments, thereby enhancing the precision of the spray-coating process. To satisfy practical control requirements, this study employs manifold deformation control methods to simulate and physically test various motion paths, verifying the accuracy and stability of the customized 7-axis suspended robotic arm control system. Additionally, trajectory-tracking performance and spray quality uniformity are assessed on actual workpieces during the spraying process. The results support a reliable solution for robotic arm control systems in automated spray production lines, particularly for large and complex workpieces.

2. Problem Description of Robotic Arm

In line with the actual needs of the manufacturer's automated spray production line, and taking into account the limitations of the workspace and the specific requirements for spraying complex workpieces, as shown in Figure 1, the manufacturer decided to design and develop a robotic arm. This robotic arm was further implemented in automated spray production lines to enhance spraying efficiency and reduce procurement costs.

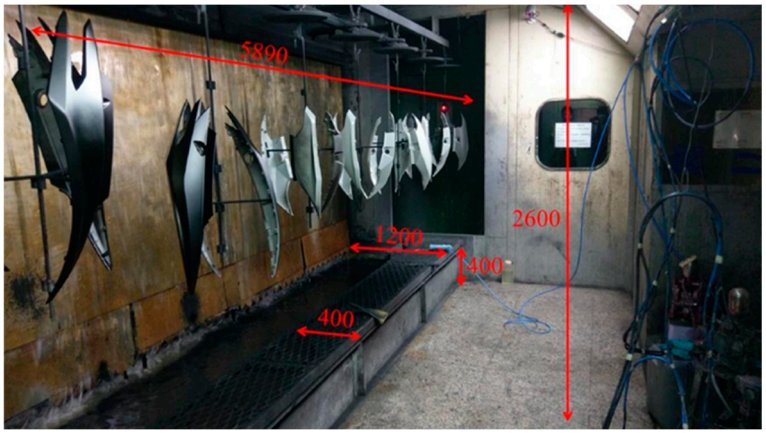

Figure 1. Dimensions of the spraying area for the robotic arm (in mm).

Based on the site and workpiece dimensions outlined in Table 1, thorough system analysis and planning have been conducted to accommodate various workpiece sizes and ensure the precise placement of the robotic arm.

Table 1. Workspace and workpiece dimensions for system analysis and robotic arm placement.

Dimensions	Length (mm)	Width (mm)	Height (mm)
Applicable workspace	1800	800	1500
Robotic arm workspace	900	700	900
Maximum size of workpiece	800	600	800
Minimum size of workpiece	440	300	120

3. Methodology for Customizing Robotic Arms

In response to the actual needs of manufacturers, the primary goal of this study is the design and customization of robotic arms. The design process and completion of these customized robotic arms are detailed as follows:

3.1. Design of 7-Axis Suspended Robotic Arm

From Table 1, to accommodate a range of workpiece sizes and ensure accurate placement of the robotic arm, careful considerations have been made to avoid specific singularities during the arm's movements. Measures have been taken to enhance the flexibility of the robotic arm's working range, allowing it to handle various complicated workpieces efficiently and without obstruction. Thus, a customized 7-axis suspended robotic arm is selected. Using the 3D-modeling software SolidWorks 2022, simulations of the endpoints of the 7-axis robotic arm are conducted to verify its ability to reach all positions within the designated working space, as shown in Figure 2.

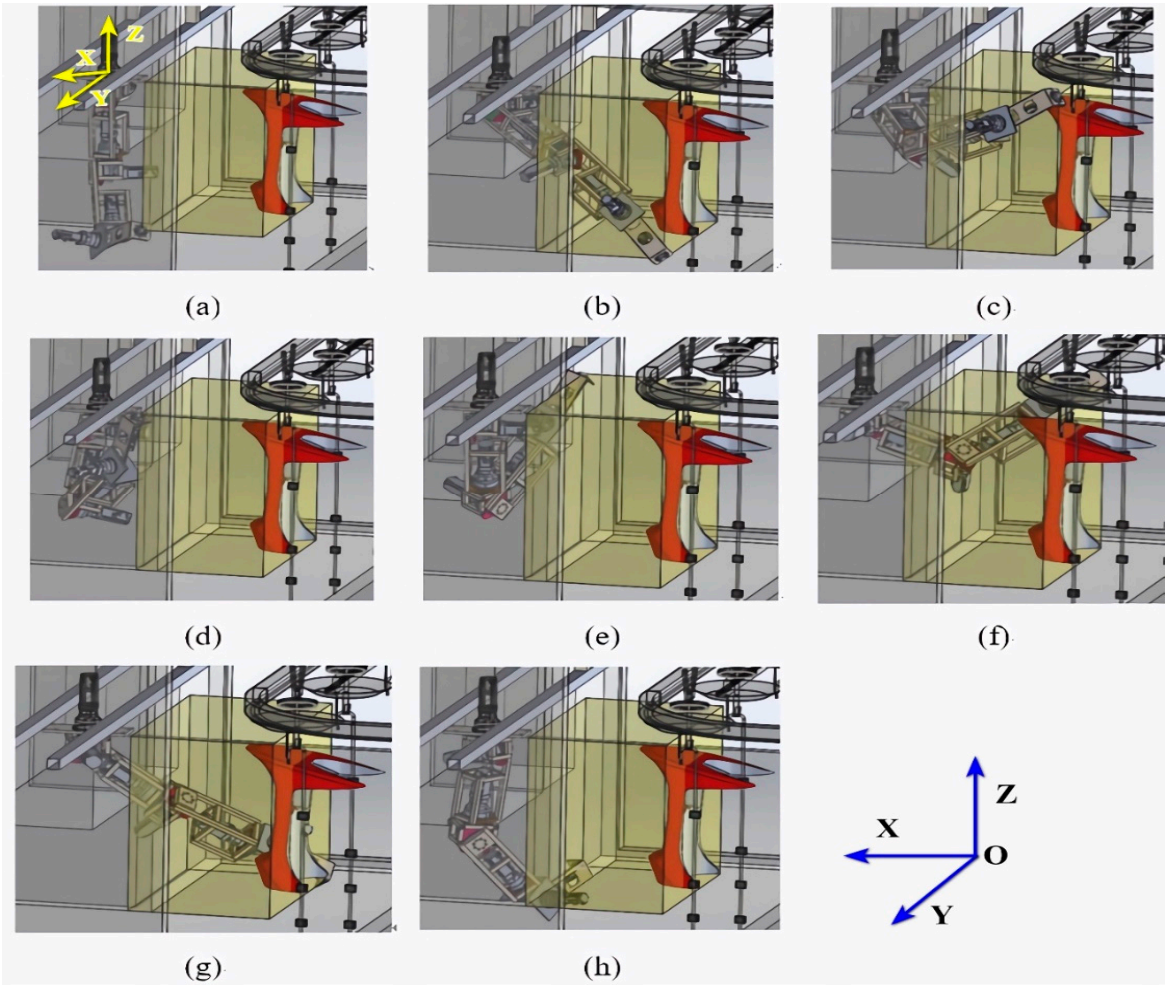

Figure 2. Three-dimensional simulation of the 7-axis robotic arm's reachability within the workspace: (**a**–**h**) correspond to the coordinates in Table 2(a–h).

Table 2. Coordinates of robotic arm movements relative to the origin point.

Coordinates	X (mm)	Y (mm)	Z (mm)
a	−1435	475	−400
b	−1435	475	−1300
c	−1435	−425	−400
d	−1435	−425	−1300
e	−735	475	−400
f	−735	−425	−400
g	−735	475	−1300
h	−735	−425	−1300

In these simulations, the coordinates of point O are defined as the origin [0, 0, 0], and the coordinates of points a through h, representing various positions achieved by the robotic arm's movements, are calculated relative to this origin. These coordinates are systematically outlined in Table 2 to facilitate precise tracking and analysis of the robotic arm's reach and movement range.

3.2. Mechanism of 7-Axis Suspended Robotic Arm

In this study, the loads on each axis of the robotic arm are calculated and analyzed to ensure the arm's performance and stability under various operating conditions, as detailed in Table 3. The load at the end effector is specified as 5 kg. During the design phase of the robotic arm mechanism, the potential impact of load variations on structural stress is carefully considered. This analysis necessitates selecting appropriate materials and incorporating structural reinforcements to guarantee the stability and durability of the robotic arm during prolonged operation. The objective is to ensure that the arm can withstand the stresses associated with varying loads without compromising its precision, efficiency, or long-term functionality.

Table 3. Load distribution across each axis of the robotic arm.

Axis Number (i = 1~7)	Mechanism Weight (kg) A_i	Motor Weight (kg) B_i	Reducer Weight (kg) C_i	Motor with Reducer Weight (kg) $D_i = B_i + C_i$	Axis Body Weight (kg) $E_i = A_i + D_i$	Axis Loading (kg) $F_i = E_{i+1} + F_{i+1}$
7th axis	3.181	0.740	1.400	2.140	5.321	5.000
6th axis	5.375	1.300	1.400	2.700	8.075	10.321
5th axis	17.557	1.300	1.400	2.700	20.257	18.396
4th axis	29.104	5.900	7.400	13.300	42.404	38.653
3rd axis	35.103	5.900	7.400	13.300	48.313	81.057
2nd axis	70.970	15.000	16.700	31.700	102.670	129.370
1st axis	75.000	15.000	16.700	31.700	106.700	232.040

where $E_8 = 0$, $F_8 =$ Weight Load $= 5$ Kg.

When designing a robotic arm, each axis must be structurally analyzed to ensure it can withstand the loads imposed during operation. These loads include the combined weight of motors, gear reducers, and payload, which act as downward forces on the robotic arm's structure. For simplicity, each axis of the robotic arm can be modeled as a cantilever beam, fixed at one end and subjected to a concentrated or distributed load. This approach enables the calculation of critical mechanical parameters such as shear force, bending moment, and section modulus, which are essential for ensuring structural integrity.

To ensure the axis can safely withstand the bending moment, the required section modulus S must be determined. The section modulus relates the bending moment to the allowable stress in the material and is given by the following [40]:

$$S = \frac{F \cdot L}{\sigma_{allowable}} = \frac{M}{\sigma_{allowable}}, \text{ and } \sigma_{allowable} = \frac{\sigma_{yield}}{\text{Safety Factor}} \quad (1)$$

Here, F represents the maximum shear force, which accounts for the total weight, including the motor, reducer, and payload. L is the length of the axis. M is the maximum bending moment. $\sigma_{allowable}$ is the allowable stress of the material. σ_{yield} is the yield strength of the material. Safety Factor is chosen based on the application and reliability requirements (typically 1.5 to 3 for robotic systems).

According to the literature [40], the properties of the square tube material and its section such as yield strength, allowable bending stress, allowable shear stress, and dimensions for carbon steel are provided. Using the cross-sectional view shown in Figure 3 and applying Equation (2), the section modulus (S') of the square tube is calculated. This calculated section modulus must exceed the value obtained from Equation (1), which defines the required section modulus for ensuring structural integrity under load. Based on the data presented in Table 3 and using the same calculation method, the appropriate section

modulus for each axis of the robotic arm is determined. This ensures that the selected square tube can adequately support the stresses and forces imposed on the robotic arm during operation, while maintaining stability and safety.

$$S' = \frac{BH^3 - bh^3}{6H} \tag{2}$$

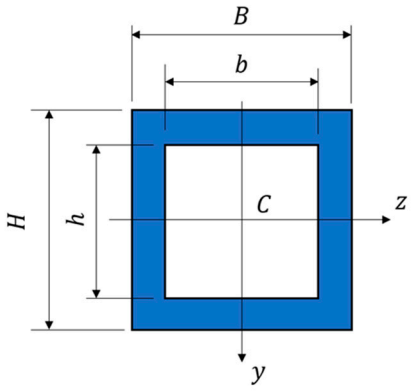

Figure 3. Cross-sectional diagram of the square tube for structural analysis.

3.3. Kinematics of 7-Axis Suspended Robotic Arm

The 7-axis suspended robotic arm consists of seven rotational joints, which provide a high degree of flexibility and maneuverability, as illustrated in Figure 4. Each joint is designed to enable precise and independent rotational movement, allowing the robotic arm to perform complex tasks within the working space. The configuration of these seven rotational joints ensures a wide range of motion, facilitates smooth transitions between positions, and helps avoid singularities during operation. For forward kinematics, the known joint angles are substituted into the transformation matrices to derive the x, y, and z coordinates of the arm in space, along with its orientation. This process allows for the determination of the end effector's position and orientation.

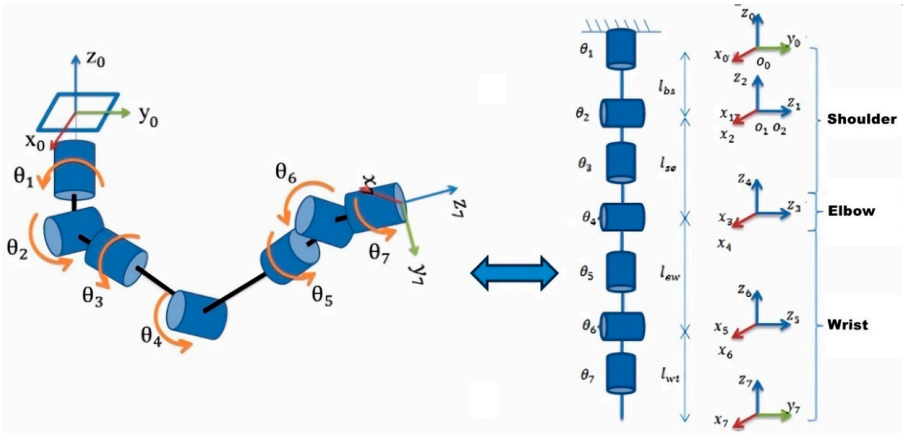

Figure 4. Configuration of the seven rotational joints in the 7-axis suspended robotic arm.

In the Denavit–Hartenberg method, the homogeneous transformation matrix is represented by four basic transformation parameters, as shown in Equation (3).

$$T_n^{n-1} = \begin{bmatrix} cos\theta_n & -sin\theta_n cos\alpha_n & \sin\theta_n \sin\alpha_n & a_n \cos\theta_n \\ sin\theta_n & cos\theta_n cos\alpha_n & -\cos\theta_n \sin\alpha_n & a_n \sin\theta_n \\ 0 & \sin\alpha_n & \cos\alpha_n & d_n \\ 0 & 0 & 0 & 1 \end{bmatrix} \tag{3}$$

Based on Figure 4, the Denavit–Hartenberg parameters are listed in Table 4, where n represent the number of the robotic arm joints (n = 1, 2, 3, …, 7), θ_n is the joint angle, a_n is the link offset distance, d_n is the link length, and α_n is the link rotation angle. These parameters are crucial for defining the kinematic relationship between the links and joints of the robotic arm, enabling the calculation of the arm's configuration and position in space.

Table 4. Denavit–Hartenberg parameters for the 7-axis suspended robotic arm kinematics.

Joint	θ_n (rad)	α_n (rad)	a_n (m)	d_n (m)
1	θ_1	$-\pi/2$	0	l_{bs}
2	θ_2	$\pi/2$	0	0
3	θ_3	$-\pi/2$	0	l_{se}
4	θ_4	$\pi/2$	0	0
5	θ_5	$-\pi/2$	0	l_{ew}
6	θ_6	$\pi/2$	0	0
7	θ_7	0	0	l_{wt}

From the 3D simulation software, the lengths of the links shown in Figure 4 are defined as follows: l_{bs} = 422 mm, l_{se} = 760 mm, l_{ew} = 516 mm, and l_{wt} = 360 mm. By substituting the parameters from Table 4 into Equations (3) and (4), we can obtain homogeneous transformation matrices for each axis.

$$
\begin{gathered}
T_1^0 = \begin{bmatrix} cos\theta_1 & 0 & -sin\theta_1 & 0 \\ sin\theta_1 & 0 & cos\theta_1 & 0 \\ 0 & -1 & 0 & l_{bs} \\ 0 & 0 & 0 & 1 \end{bmatrix}, T_2^1 = \begin{bmatrix} cos\theta_2 & 0 & sin\theta_2 & 0 \\ sin\theta_2 & 0 & -cos\theta_2 & 0 \\ 0 & 1 & 0 & 0 \\ 0 & 0 & 0 & 1 \end{bmatrix} \\
T_3^2 = \begin{bmatrix} cos\theta_3 & 0 & -sin\theta_3 & 0 \\ sin\theta_3 & 0 & cos\theta_3 & 0 \\ 0 & -1 & 0 & l_{se} \\ 0 & 0 & 0 & 1 \end{bmatrix}, T_4^3 = \begin{bmatrix} cos\theta_4 & 0 & sin\theta_4 & 0 \\ sin\theta_4 & 0 & -cos\theta_4 & 0 \\ 0 & 1 & 0 & 0 \\ 0 & 0 & 0 & 1 \end{bmatrix} \\
T_5^4 = \begin{bmatrix} cos\theta_5 & 0 & -sin\theta_5 & 0 \\ sin\theta_5 & 0 & cos\theta_5 & 0 \\ 0 & -1 & 0 & l_{ew} \\ 0 & 0 & 0 & 1 \end{bmatrix}, T_6^5 = \begin{bmatrix} cos\theta_6 & 0 & sin\theta_6 & 0 \\ sin\theta_6 & 0 & -cos\theta_6 & 0 \\ 0 & 1 & 0 & 0 \\ 0 & 0 & 0 & 1 \end{bmatrix} \\
T_7^6 = \begin{bmatrix} cos\theta_7 & -sin\theta_7 & 0 & 0 \\ sin\theta_7 & cos\theta_7 & 0 & 0 \\ 0 & 1 & 1 & l_{wt} \\ 0 & 0 & 0 & 1 \end{bmatrix}
\end{gathered} \tag{4}
$$

By multiplying the homogeneous transformation matrices from Equations (4) and (5), the position and orientation of the end effect can be derived.

$$
T_7^0 = T_1^0 T_2^1 T_3^2 T_4^3 T_5^4 T_6^5 T_7^6 = \begin{bmatrix} r_{11} & r_{12} & r_{13} & p_x \\ r_{21} & r_{22} & r_{23} & p_y \\ r_{31} & r_{32} & r_{33} & p_z \\ 0 & 0 & 0 & 1 \end{bmatrix} \tag{5}
$$

Each parameter in Equation (5) is listed as follows from Equations (6)–(17). The position and orientation of coordinate frame 7 relative to the origin can be determined by substituting the values from Equations (6)–(17) into Equation (5).

s_$s_n = sin\theta_n$ and $c_n = cos\theta_n (n = 1, 2, 3, \ldots, 7)$ are used in the symbol explanation for Equations (6)–(17).

$$r_{11} = c_7 * (s_6 * (s_4 * (s_1 * s_3 - c_1 * c_2 * c_3) - c_1 * c_4 * s_2) - c_6 * (c_5 * (c_4 * (s_1 * s_3 - c_1 * c_2 * c_3) + c_1 * s_2 * s_4) + s_5 * (c_3 * s_1 + c_1 * c_2 * s_3))) + s_7 * (s_5 * (c_4 * (s_1 * s_3 - c_1 * c_2 * c_3) + c_1 * s_2 * s_4) - c_5 * (c_3 * s_1 + c_1 * c_2 * s_3)) \quad (6)$$

$$r_{21} = -c_7 * (s_6 * (s_4 * (c_1 * s_3 + c_2 * c_3 * s_1) + c_4 * s_1 * s_2) - c_6 * (c_5 * (c_4 * (c_1 * s_3 + c_2 * c_3 * s_1) - s_1 * s_2 * s_4) + s_5 * (c_1 * c_3 - c_2 * s_1 * s_3))) - s_7 * (s_5 * (c_4 * (c_1 * s_3 + c_2 * c_3 * s_1) - s_1 * s_2 * s_4) - c_5 * (c_1 * c_3 - c_2 * s_1 * s_3)) \quad (7)$$

$$r_{31} = s_7 * (s_5 * (c_2 * s_4 + c_3 * c_4 * s_2) + c_5 * s_2 * s_3) - c_7 * (c_6 * (c_5 * (c_2 * s_4 + c_3 * c_4 * s_2) - s_2 * s_3 * s_5) + s_6 * (c_2 * c_4 - c_3 * s_2 * s_4)) \quad (8)$$

$$r_{12} = c_7 * (s_5 * (c_4 * (s_1 * s_3 - c_1 * c_2 * c_3) + c_1 * s_2 * s_4) - c_5 * (c_3 * s_1 + c_1 * c_2 * s_3)) - s_7 * (s_6 * (s_4 * (s_1 * s_3 - c_1 * c_2 * c_3) - c_1 * c_4 * s_2) - c_6 * (c_5 * (c_4 * (s_1 * s_3 - c_1 * c_2 * c_3) + c_1 * s_2 * s_4) + s_5 * (c_3 * s_1 + c_1 * c_2 * s_3))) \quad (9)$$

$$r_{22} = s_7 * (s_6 * (s_4 * (c_1 * s_3 + c_2 * c_3 * s_1) + c_4 * s_1 * s_2) - c_6 * (c_5 * (c_4 * (c_1 * s_3 + c_2 * c_3 * s_1) - s_1 * s_2 * s_4) + s_5 * (c_1 * c_3 - c_2 * s_1 * s_3))) - c_7 * (s_5 * (c_4 * (c_1 * s_3 + c_2 * c_3 * s_1) - s_1 * s_2 * s_4) - c_5 * (c_1 * c_3 - c_2 * s_1 * s_3)) \quad (10)$$

$$r_{32} = c_7 * (s_5 * (c_2 * s_4 + c_3 * c_4 * s_2) + c_5 * s_2 * s_3) + s_7 * (c_6 * (c_5 * (c_2 * s_4 + c_3 * c_4 * s_2) - s_2 * s_3 * s_5) + s_6 * (c_2 * c_4 - c_3 * s_2 * s_4)) \quad (11)$$

$$r_{13} = -c_6 * (s_4 * (s_1 * s_3 - c_1 * c_2 * c_3) - c_1 * c_4 * s_2) - s_6 * (c_5 * (c_4 * (s_1 * s_3 - c_1 * c_2 * c_3) + c_1 * s_2 * s_4) + s_5 * (c_3 * s_1 + c_1 * c_2 * s_3)) \quad (12)$$

$$r_{23} = c_6 * (s_4 * (c_1 * s_3 + c_2 * c_3 * s_1) + c_4 * s_1 * s_2) + s_6 * (c_5 * (c_4 * (c_1 * s_3 + c_2 * c_3 * s_1) - s_1 * s_2 * s_4) + s_5 * (c_1 * c_3 - c_2 * s_1 * s_3)) \quad (13)$$

$$r_{33} = c_6 * (c_2 * c_4 - c_3 * s_2 * s_4) - s_6 * (c_5 * (c_2 * s_4 + c_3 * c_4 * s_2) - s_2 * s_3 * s_5) \quad (14)$$

$$p_x = l_{se} * c_1 * s_2 - l_{wt} * (c_6 * (s_4 * (s_1 * s_3 - c_1 * c_2 * c_3) - c_1 * c_4 * s_2) + s_6 * (c_5 * (c_4 * (s_1 * s_3 - c_1 * c_2 * c_3) + c_1 * s_2 * s_4) + s_5 * (c_3 * s_1 + c_1 * c_2 * s_3))) - l_{ew} * (s_4 * (s_1 * s_3 - c_1 * c_2 * c_3) - c_1 * c_4 * s_2) \quad (15)$$

$$p_y = l_{ew} * (s_4 * (c_1 * s_3 + c_2 * c_3 * s_1) + c_4 * s_1 * s_2) + l_{wt} * (c_6 * (s_4 * (c_1 * s_3 + c_2 * c_3 * s_1) + c_4 * s_1 * s_2) + s_6 * (c_5 * (c_4 * (c_1 * s_3 + c_2 * c_3 * s_1) - s_1 * s_2 * s_4) + s_5 * (c_1 * c_3 - c_2 * s_1 * s_3))) + l_{se} * s_1 * s_2 \quad (16)$$

$$p_z = l_{bs} + c_2 * l_{se} - l_{wt} * (s_6 * (c_5 * (c_2 * s_4 + c_3 * c_4 * s_2) - s_2 * s_3 * s_5) - c_6 * (c_2 * c_4 - c_3 * s_2 * s_4)) + l_{ew} * (c_2 * c_4 - c_3 * s_2 * s_4) \quad (17)$$

In the inverse kinematics analysis of the 7-axis suspended robotic arm, as described in references [41–43], the orientation schematic is depicted in Figure 5. This schematic illustrates the spatial relationship between the robotic arm's end effector and its joints, providing a visual representation of the arm's configuration in three-dimensional space. The schematic serves as a basis for deriving the inverse kinematics equations, which are used to determine the joint angles required to position the end effector at a specified location with a given orientation. By using this orientation model, the inverse kinematics analysis allows for precise control of the robotic arm's movements, ensuring that the end effector can reach desired positions and orientations within the workspace.

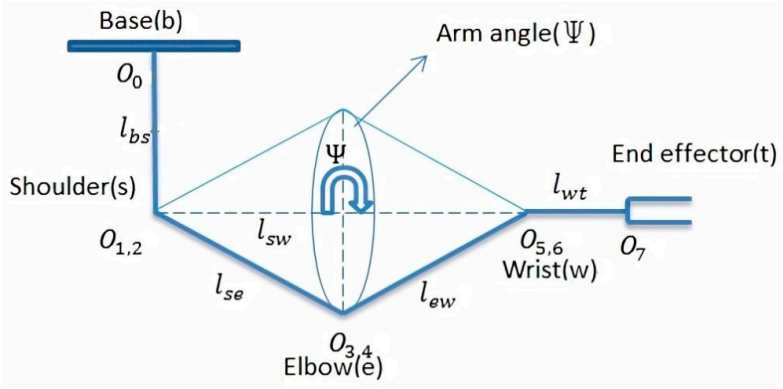

Figure 5. Orientation schematic for inverse kinematics analysis of the 7-axis robotic arm [43].

The suspended 7-axis robotic arm is parameterized by defining the arm angle as the angle between the reference plane and the arm plane. The arm plane is defined as the plane passing through the shoulder, elbow, and wrist joints. The reference plane is established by setting the angle of joint 3 to zero, which aligns the axes of rotation for joints 2 and 4 to be parallel. In this non-redundant configuration, the plane formed by the shoulder, elbow, and wrist serves as the reference plane. The coordinates of the wrist point w are calculated as shown in Equation (18).

$$\mathrm{w} = \begin{bmatrix} w_x \\ w_y \\ w_z \end{bmatrix} = P_7^b - l_{wt} R_7^b \begin{bmatrix} 0 \\ 0 \\ 1 \end{bmatrix} \tag{18}$$

Here, P_7^b represents the position vector of the 7th axis (O_7) relative to the base (b), R_7^b represents the rotation matrix of the 7th axis (O_7) relative to the base (b), and l_{wt} denotes the link length from the wrist to the 7th axis (O_7).

To calculate the position vector of the wrist relative to the shoulder, use Equation (19).

$$L_w^s = w - L_s^b \tag{19}$$

$$L_s^b = \begin{bmatrix} 0 \\ 0 \\ l_{bs} \end{bmatrix} \tag{20}$$

From the given orientation, the position of the end effector is determined, followed by calculating the wrist position. Since all variables on the right-hand side of Equation (19) are constants relative to the fixed base, the line l_{sw}, which connects the shoulder to the wrist, remains fixed. As shown in Figure 5, a rotation matrix must be derived to represent the free rotational arm angle ψ about the axis connecting the shoulder and wrist. Rodrigues' rotation formula is an efficient algorithm for representing rotation vectors in space. Given l_{sw} and the rotation angle ψ, the following Equation (21) can be derived:

$$R_\Psi = I + (1 - \cos(\psi))k_w^{s\,2} + \sin(\psi)k_w^s \tag{21}$$

where

$$I = \begin{bmatrix} 1 & 0 & 0 \\ 0 & 1 & 0 \\ 0 & 0 & 1 \end{bmatrix} \tag{22}$$

and

$$k_w^s = \begin{bmatrix} 0 & -u_w^s(z) & u_w^s(y) \\ u_w^s(z) & 0 & -u_w^s(x) \\ -u_w^s(y) & u_w^s(x) & 0 \end{bmatrix}. \tag{23}$$

In Equations (22) and (23), u_w^s is the unit vector of L_w^s, which can be obtained from Equation (24).

$$u_w^s = \frac{\mathrm{L}_w^s}{\|\mathrm{L}_w^s\|} \tag{24}$$

Here, L_w^s represents the position vector of the wrist relative to the shoulder.

As previously mentioned, the wrist position is unaffected by any arm angle. From the base of the arm, the orientation of the spherical joint at the wrist varies with different arm angles. In Figure 6, the angle of joint 4 is independent of the arm angle, meaning that the position of joint 4 does not directly depend on the overall orientation of the arm. However, adjusting the arm angle influences the orientation of the spherical joint at the shoulder. This effect can be quantified using the following equation, which relates the arm's angle to the orientation of the shoulder joint.

$$R_3^0 = R_\psi R_3^{0'} \tag{25}$$

where $R_3^{0'}$ is the shoulder rotation matrix when the third joint angle is assumed to be zero and the arm angle is also zero.

$$\|L_w^s\|^2 = {l_{se}}^2 + {l_{ew}}^2 - 2l_{se}l_{ew}\cos\left({\theta'}_4\right) \tag{26}$$

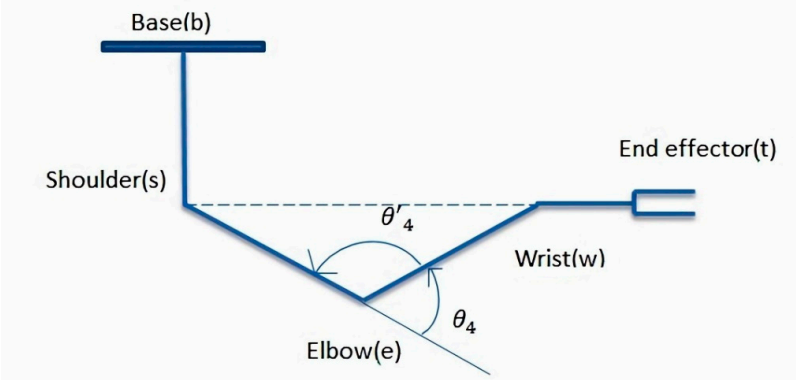

Figure 6. Orientation and rotation axis of joint 4 in the 7-axis robotic arm.

$$\cos\left({\theta'}_4\right) = \frac{{l_{se}}^2 + {l_{ew}}^2 - \|L_w^s\|^2}{2l_{se}l_{ew}} \tag{27}$$

$$\theta_4 = \pi - {\theta'}_4 \tag{28}$$

The shoulder joint angle is determined by the defined arm angle, as shown in Equation (25). While maintaining a fixed posture, the reference plane is first established, and then the shoulder joint angle is calculated by adjusting the arm angle. Through mathematical derivations, based on the new robot arm angle parameter ψ, the seven joint angle values of the 7-axis suspended robotic arm for spraying can be calculated as follows:

$$\mathrm{X}_S = k_w^s R_3^{0'} = \begin{bmatrix} \mathrm{X}_{s11} & \mathrm{X}_{s12} & \mathrm{X}_{s13} \\ \mathrm{X}_{s21} & \mathrm{X}_{s22} & \mathrm{X}_{s23} \\ \mathrm{X}_{s31} & \mathrm{X}_{s32} & \mathrm{X}_{s33} \end{bmatrix} \tag{29}$$

$$\mathrm{Y}_S = -\left({k_w^s}^2\right) R_3^{0'} = \begin{bmatrix} \mathrm{Y}_{s11} & \mathrm{Y}_{s12} & \mathrm{Y}_{s13} \\ \mathrm{Y}_{s21} & \mathrm{Y}_{s22} & \mathrm{Y}_{s23} \\ \mathrm{Y}_{s31} & \mathrm{Y}_{s32} & \mathrm{Y}_{s33} \end{bmatrix} \tag{30}$$

$$Z_S = \left(I + k_w^{s\,2}\right) R_3^{0\prime} = \begin{bmatrix} Z_{s11} & Z_{s12} & Z_{s13} \\ Z_{s21} & Z_{s22} & Z_{s23} \\ Z_{s31} & Z_{s32} & Z_{s33} \end{bmatrix} \tag{31}$$

$$\theta_1 = \text{atan}\left(\frac{-S_\psi X_{s22} - C_\psi Y_{s22} - Z_{s22}}{-S_\psi X_{s12} - C_\psi Y_{s12} - Z_{s12}}\right) \tag{32}$$

$$\theta_2 = \text{acos}\left(-S_\psi X_{s32} - C_\psi Y_{s32} - Z_{s32}\right) \tag{33}$$

$$\theta_3 = \text{atan}\left(\frac{S_\psi X_{s33} + C_\psi Y_{s33} + Z_{s33}}{-S_\psi X_{s31} - C_\psi Y_{s31} - Z_{s31}}\right) \tag{34}$$

$$\theta_5 = \text{atan}\left(\frac{S_\psi X_{w23} - C_\psi Y_{w23} - Z_{w23}}{-S_\psi X_{w13} - C_\psi Y_{w13} - Z_{w13}}\right) \tag{35}$$

$$\theta_6 = \text{acos}\left(-S_\psi X_{w33} - C_\psi Y_{w33} - Z_{w33}\right) \tag{36}$$

$$\theta_7 = \text{atan}\left(-\frac{S_\psi X_{w32} + C_\psi Y_{w32} + Z_{w32}}{S_\psi X_{w31} + C_\psi Y_{w31} + Z_{w31}}\right) \tag{37}$$

The mathematical symbols in Equations (29)–(37), such as $S_\psi (= \sin(\psi))$, $C_\psi (= \cos(\psi))$, $X_{s12}\ldots$ etc., represent mathematical operations used in the derivation process.

3.4. System Architecture of 7-Axis Suspended Robotic Arm

The completed customized 7-axis suspended robotic arm setup includes a computer, a digital I/O interface card, a multi-axis servo control board with an embedded manifold deformation controller, and the controlled body. Each rotating axis utilizes Mitsubishi MR-J4 series AC servo motors, paired with reducers to enhance output torque. The position signals from the motors are processed using pulse incremental encoders associated with the AC servo motors. The computer system is utilized to calculate the necessary control commands, which are then processed and transmitted by the control board developed in the laboratory. This control board communicates directly with the driver to execute the commands and regulate the robotic arm's movements. The system architecture diagram of the entire setup is presented in Figure 7, providing a detailed overview of how each component interacts within the control system. The diagram illustrates the flow of information from the computer through the control board to the driver, ensuring accurate and synchronized operation of the robotic arm.

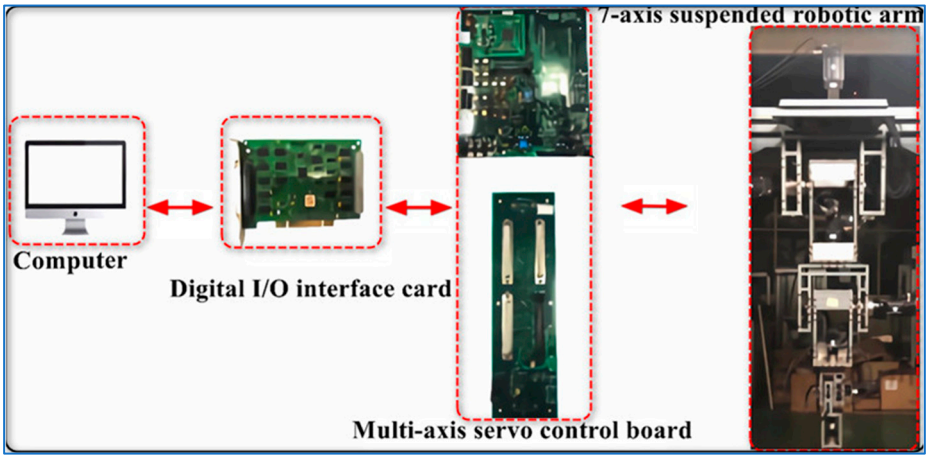

Figure 7. System architecture of the 7-axis suspended robotic arm control system.

3.5. System Identification of 7-Axis Suspended Robotic Arm

The dynamics of a robotic arm with n links and rotating joints can be described as follows [41]:

$$\mathrm{M}(\theta)\ddot{\theta} + f\left(\theta, \dot{\theta}\right) + g(\theta) = \tau + \tau_f \tag{38}$$

Here, θ is the $n \times 1$ joint coordinate vector, $\mathrm{M}(\theta)$ is the $n \times n$ inertia matrix, $f\left(\theta, \dot{\theta}\right)$ is the $n \times 1$ vector of centrifugal and Coriolis forces, and $g(\theta)$ is the gravity vector. τ is the input torque vector and τ_f is the disturbance torque vector.

The robotic arm system is a non-linear, coupled, and time-varying system. To design the controller, system identification methods are required for processing and validation. The main purpose of system identification is to ensure that the control system performs well, thereby reducing the load on the controller. This is achieved by designing the control laws based on the system model, which needs to be identified through experiments. In this study, the time-domain system identification method is employed, where a step input signal is applied to the system, and the system identification is conducted based on its step response graph. Here, the identification is focused on the seven servo motor systems. Multiple system identification processes are performed for each axis to obtain the reference linear system parameters. Assume that each axis is a second-order linear system.

The state-space representation can be written as follows:

$$\begin{cases} \dot{x}_1 = x_2 \\ \dot{x}_2 = -a_2 x_2 - a_1 x_1 - b\dot{u} \end{cases} \tag{39}$$

Let

$$\begin{aligned} \dot{x}_1 &= y_d - y \\ x_2 &= -\dot{y} \end{aligned} \tag{40}$$

Equation (39) can be rearranged and written as follows:

$$\ddot{y} + a_2\dot{y} + a_1 y = bu \tag{41}$$

where

$$u = K_p x_1 = K_p(y_d - y) = K_p y_d - K_p y \tag{42}$$

Substituting Equation (42) into Equation (41), rearranging, and then applying the Laplace Transform yields the following:

$$\frac{Y}{Y_d} = \frac{a_1 + bK_p}{S^2 + a_2 S + \left(a_1 + bK_p\right)} = \frac{\omega_n^2}{S^2 + 2\xi\omega_n S + \omega_n^2} \tag{43}$$

When $K_p = 1$, Equation (43) can be rewritten as follows:

$$\frac{Y}{Y_d} = \frac{a_1 + b}{S^2 + a_2 S + (a_1 + b)} = \frac{\omega_n^2}{S^2 + 2\xi\omega_n S + \omega_n^2} \tag{44}$$

Here, Y_d represents the input control target, $a_1, a_2,\ b$ represent identification parameters, ξ is the damping ratio, and ω_n is the natural frequency.

When the arm is in the origin position, system identification is performed for each axis. Taking the first axis as an example, a step signal is applied as the input to the system. By analyzing the step response, shown in Figure 8, the response process after the system receives the step signal can be observed and analyzed. These identification parameters are crucial for understanding the behavior of each axis and optimizing the control system. The calculated parameters are summarized in Table 5, which provides a clear representation of the system's dynamic characteristics for each axis.

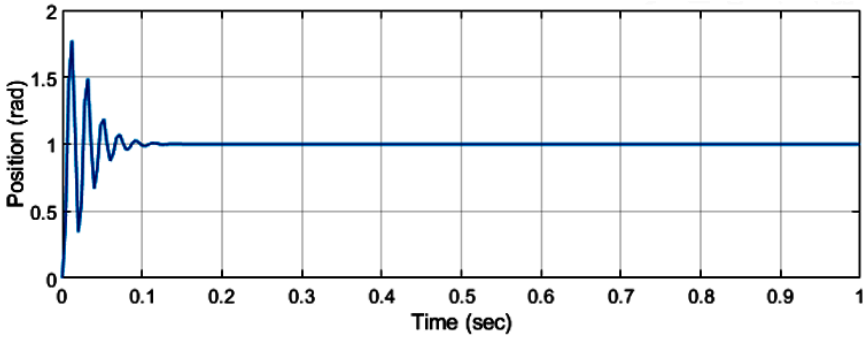

Figure 8. Step response diagram for system identification of the first axis.

Table 5. Calculated parameters from step response analysis.

Parameter Name	Symbols and Calculations	Values
Peak time	t_p	0.012 (s)
Value of max peak Final value	M_p 1	1.772 (rad) 1.000 (rad)
Percent maximum overshoot	$\mathrm{P.O}(\%) = 100\frac{M_p - F_v}{F_v}$	77.250
Damping ratio	$\xi = -\ln(P.O/100)/sqrt(\pi^2 + ln^2(\frac{P.O}{100}))$	0.080
Damped natural frequency	$\omega_d = \frac{2\pi}{\Delta t}$ Δt = 0.02 s (the time interval between two consecutive peaks)	314.160
Natural frequency	$\omega_n = \frac{\omega_d}{\sqrt{1-\xi^2}}$	315.220

Using the identification quantities derived in Table 5, the system performance parameters a_1, a_2, and b can be calculated.

Similarly, using the calculation method for axis 1, the remaining six axes can be identified, enabling the determination of system performance parameter values for axis 2 through 7, as shown in Table 6. When the robotic arm moves to another position, the system identification for each axis can be recalculated using the same method to obtain updated system performance parameters (Table 5). In this study, the identification parameters are determined as the average of those calculated for the robotic arm in its original position and in another position, as illustrated in Table 6. This approach ensures a more accurate representation of the system's dynamic characteristics by accounting for potential variations in performance across different configurations.

Table 6. Averaged identification parameters for each axis of the robotic arm.

Identification Parameter		1st Axis	2nd Axis	3rd Axis	4th Axis	5th Axis	6th Axis	7th Axis
The origin position	a_1	27.49	30.27	32.08	26.85	24.96	10.11	9.80
	a_2	51.61	118.80	172.41	199.16	212.36	82.94	109.18
	b	11,040.38	12,778.80	15,161.34	13,076.1	9965.6	5278.8	5843.03
Another position	a_1	47.82	28.41	30.83	24.09	25.44	14.83	11.89
	a_2	336.44	71.96	262.84	287.34	240.94	109.18	115.27
	b	21,973.4	2078.33	16,473.30	12,901.37	13,842.1	5843.03	9083.61
The average values	a_1	37.66	29.34	31.46	25.47	25.20	12.47	10.85
	a_2	194.03	95.38	217.635	243.25	226.65	96.06	112.23
	b	16,506.89	7428.57	15,817.32	12,988.74	11,433.49	5560.92	7463.32

3.6. Control System of 7-Axis Suspended Robotic Arm

In this study, the control system for the 7-axis suspended robotic arm employs the Manifold Deformation Design Scheme (MDDS) proposed by C.S. Liu et al. [44,45]. This method combines smoothness and robustness in closed-loop control, utilizing the dynamic behavior of the system mapped to the system's state space for control. Within the state space, the action process is designed as a reference behavior for the system's dynamics. The current state feedback from the closed-loop system is compared with the reference behavior, and the control output is calculated to gradually align the system's behavior with the pre-defined action process. In practical mechanical systems, disturbances caused by physical factors such as gravity, friction, and inertia can hinder the controlled system's ability to accurately reach the target state. The manifold deformation control method can predict the next sampling time based on the current system state, determining the expected state behavior. If there is a discrepancy between the current system state and the predicted state from the previous sampling time, the controller can compensate the control output in real-time. This allows the system to overcome the differences caused by disturbances, ensuring stable behavior and achieving the designed target state.

The 7-axis suspended robotic arm has seven actuated axes that need to be controlled.

The block diagram of the manifold deformation controller for the i-th axis is shown in Figure 9. This controller is designed to manage the dynamic behavior of the robotic arm, specifically addressing the deformation and deflection of the arm's structure during movement.

$$\mathrm{u(kh)} = -\frac{f(x(kh))}{b} - \frac{\sum_{n=1}^{n-1} c_i[x_i(kh) + h{\cdot}x_{i+1}(kh)] + x_n(kh)}{b{\cdot}h} + u_{es}(kh) \tag{45}$$

where

$$u_{es}(kh) = u_{es}(kh-h) - \frac{x_n(kh) - x_n^*(kh)}{(b{\cdot}h)} \tag{46}$$

$$x_n^*(kh+h) = -\sum_{i=1}^{n-1} c_i[x_i(kh) + h{\cdot}x_{i+1}(kh)] \tag{47}$$

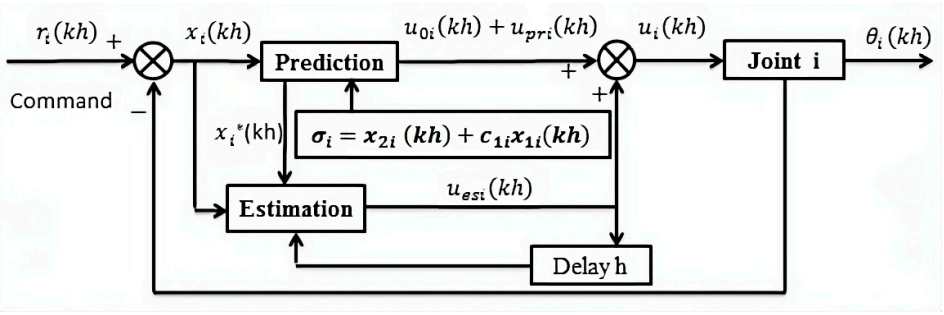

Figure 9. Block diagram of the manifold deformation controller for the i-th axis.

4. Trajectory Simulation and Experimental Control of Customized Robotic Arm

4.1. Simulation Control of Trajectories for 7-Axis Suspended Robotic Arm

To apply the customized 7-axis suspended robotic arm in an automated spraying production line, accurate control of its mobility is essential. After completing the motion tests for each axis and system identification, spatial spraying motion simulations are conducted. Initially, the path in a rectangular coordinate system is planned, and the inverse kinematics is used to determine the angle paths for each axis, which are then utilized for simulation control. The obtained control results are converted back to the rectangular coordinate path values using forward kinematics, and the error values are compared with the originally planned paths. The simulation tests are conducted using MATLAB for

analysis, incorporating the manifold deformation control method along with disturbances to track the 7-axis movement trajectory. The spraying tracking types include rectangular and circular trajectories. Additionally, a motorcycle shell provided by the manufacturer is used for tracking the spraying trajectory, as shown in Figure 10. The simulation conditions for the three trajectory-tracking types are detailed in Table 7.

Figure 10. Three-dimensional model and physical body of the motorcycle shell for spraying trajectory tracking.

Table 7. Simulation parameters for tracking control of three trajectory types.

Relevant Parameters	Rectangular Path	Circular Path	Motorcycle Shell Path
Initial Coordinates of the Robotic Arm End Effector (mm)	[0, 0, −2228]	[0, 0, −2228]	[0, 0, −2228]
Starting Coordinates of Robotic Arm (mm)	[−900, 250, −1700]	[−750, −400, −1400]	[−1094, −84.34, −2677]
Ending Coordinates of Robotic Arm (mm)	[−900, 250, −1700]	[−750, −400, −1400]	[−1227, −216.6, −674.2]
Rectangular Length (mm)	500	X	X
Circular Radius (mm)	X	400	X
Physical Workpiece Path	X	X	Planning Path Coordinates
Control Sampling Rate (Hz)	250	250	250
Manifold Deformation Control Parameters	20	20	20
Simulation Disturbance Function	$4\ \sin(4\pi t)$	$4\ \sin(4\pi t)$	$4\ \sin(4\pi t)$

From Figure 11a, using the condition of the rectangular path in Table 7, the simulated results for the robotic arm tracking a rectangular spraying trajectory are depicted in Figure 12a. During the simulation process, minor oscillations in the error values of the X, Y, and Z axes can be observed. However, these values remain close to a straight line, indicating that the simulation errors for all three axes are minimal. Similarly, under the condition of the circular path in Table 7, for the circular spraying trajectory shown in Figure 11b, the tracking results for the X, Y, and Z axes display slightly more pronounced oscillations compared to the rectangular trajectory. Nonetheless, the error values are still small, demonstrating effective trajectory tracking by the robotic arm in both simulated conditions. Furthermore, a motorcycle shell is used for tracking the spraying trajectory in Figure 10. The planned path coordinates are input into MATLAB for 7-axis inverse kinematics calculations, utilizing the 3D model of the motorcycle shell. The calculated angles for the seven axes are obtained under the simulation conditions outlined in Table 6, with the trajectory graph shown in Figure 11c. The simulation results under the condition of the motorcycle shell path in Table 7 reveal that the oscillations in the X, Y, and Z

axes throughout this simulation process is similar with both the rectangular and circular spraying trajectories; however, the overall error values are still minimal in Figure 12b.

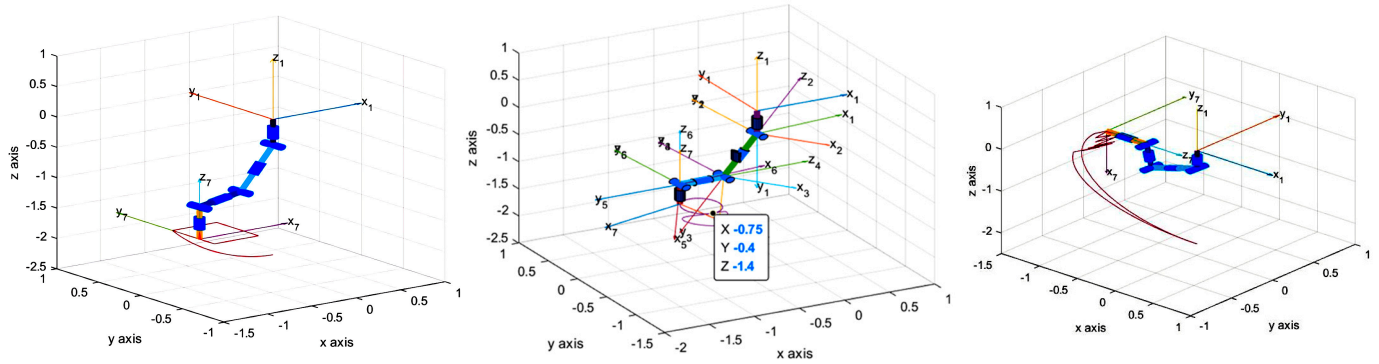

(**a**) (**b**) (**c**)

Figure 11. Simulated spray tracking trajectories: (**a**) rectangular, (**b**) circular, and (**c**) motorcycle shell.

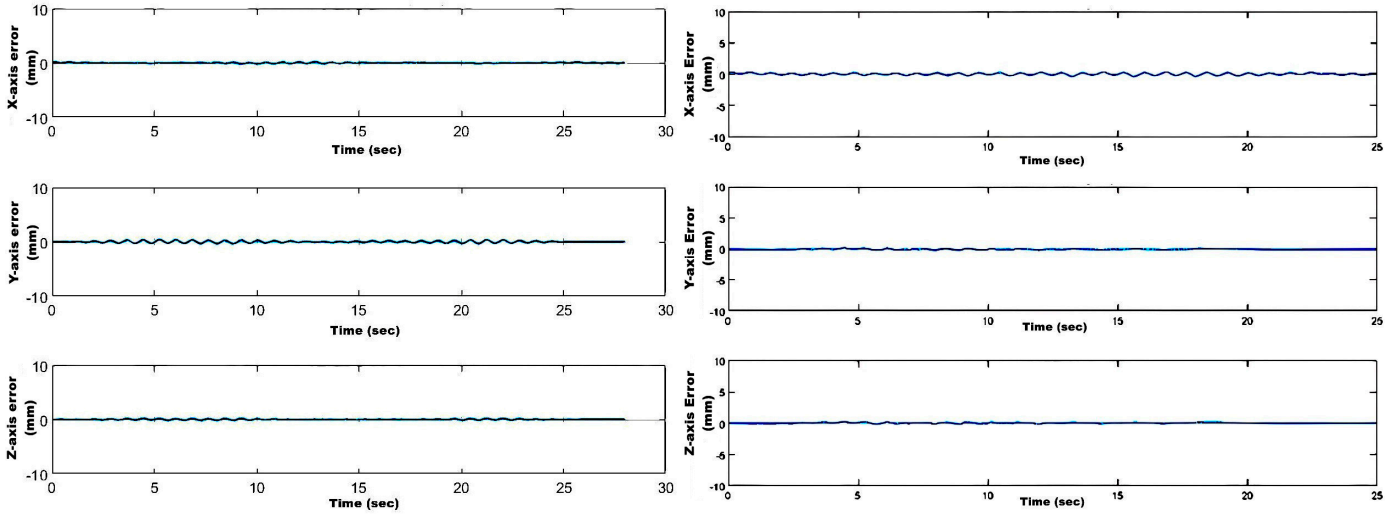

(**a**) (**b**)

Figure 12. Position error in X, Y, and Z axes during simulation control: (**a**) rectangular path, (**b**) motorcycle shell path.

The simulation results for the rectangular, circular, and motorcycle shell trajectories demonstrate that all paths can be accurately controlled to follow the specified trajectories. Further analysis of Table 8 shows that the maximum error values across all three-dimensional rectangular coordinates in the simulations are below 0.20 mm. This indicates that the manifold deformation control method provides exceptional control performance. Consequently, the 7-axis suspended robotic arm developed in this study will employ this control method in conjunction with the 7-axis servo control board for physical testing, allowing for a detailed understanding of its operational characteristics.

Table 8. Maximum error values for tracking simulation of three trajectory types.

Types	X-Axis	Y-Axis	Z-Axis
Rectangular trajectory (mm)	±0.10	±0.20	±0.09
Circular trajectory (mm)	±0.20	±0.20	±0.20
Motorcycle shell trajectory (mm)	±0.20	±0.10	±0.20

4.2. Experiment Control of Trajectories for 7-Axis Suspended Robotic Arm

The robotic arm performs experiments using the joint angles based on previously simulated spray-coating paths, such as rectangular, circular, and motorcycle shell trajectories. A projector can be installed on the robotic arm's end effector to project light onto the planned path. During the motion process, the three-dimensional path values in the Cartesian coordinate system cannot be directly measured. However, the joint angles of the seven axes can be fed back and used to compute the corresponding path values in the Cartesian coordinate system via forward kinematics. These calculated values are then compared with the initially planned path to assess the accuracy of the robotic arm's control. When the robotic arm executes a 50 cm rectangular trajectory, as shown in Figure 13, the projected light accurately follows the planned path. Similarly, when the robotic arm performs a 40 cm circular trajectory, as shown in Figure 14, the projected light also accurately follows the planned path.

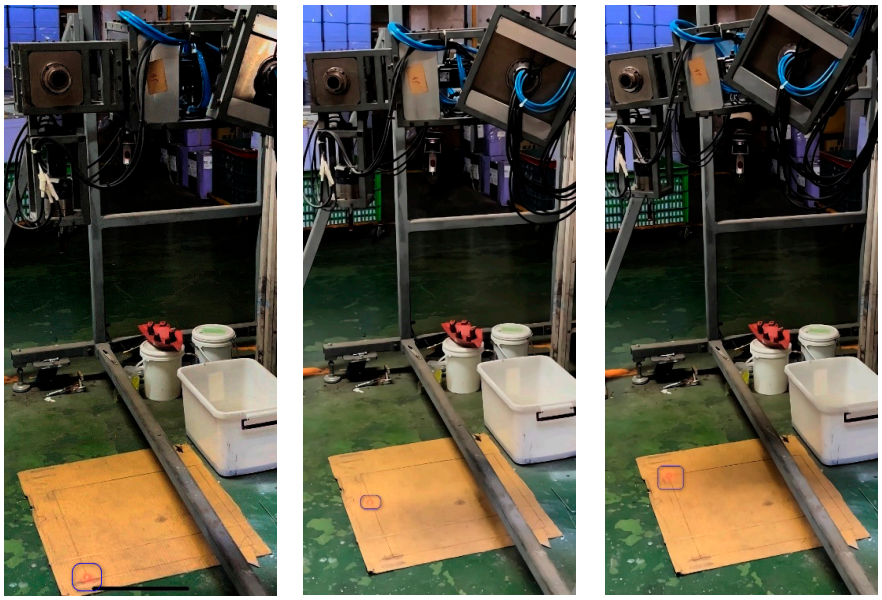

(**a**) (**b**) (**c**)

Figure 13. Continuous motion of the robotic arm along the rectangular trajectory from (**a**–**c**).

(**a**) (**b**) (**c**)

Figure 14. Continuous motion of the robotic arm along the circular trajectory from (**a**–**c**).

A spray gun has been added to the end effector of the robotic arm, with specifications that meet the manufacturer's equipment requirements. The spray gun's movement speed and the distance from the spray gun to the workpiece are set according to the manufacturer's specifications. Using the workpiece provided by the motorcycle shell as shown in Figure 10, the angles for each axis from the previously simulated trajectory are applied as

the actual angles for the robotic arm. This allows for control of the robotic arm's actual spraying trajectory, as depicted in Figure 15.

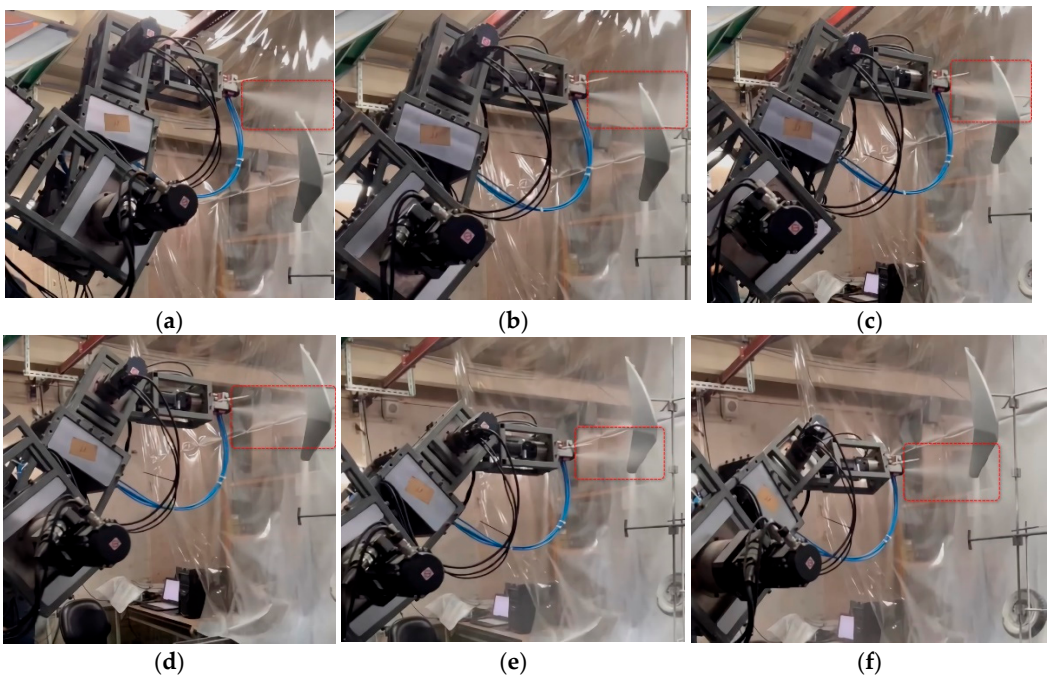

Figure 15. Continuous motion of the robotic arm along the motorcycle shell trajectory from (**a**–**f**).

In all trajectory experiments, whether rectangular, circular, or motorcycle-shell-shaped, the feedback from the 7-axis robotic arm's joint angles can be used to transform the three-dimensional path values into the Cartesian coordinate system. These values can then be compared with the originally planned path. The results in Table 9 indicate that during the experiments for the rectangular, circular, and motorcycle shell trajectory tracking, the maximum error values for the three-dimensional coordinates of the X, Y, and Z axes are all below 0.40 mm. This study demonstrates that the 7-axis suspended robotic arm developed using the manifold deformation control method can accurately perform spraying movements along the specified spraying trajectories.

Table 9. Maximum tracking error for three types of trajectory experiments.

Types	X-Axis	Y-Axis	Z-Axis
Rectangular trajectory (mm)	±0.20	±0.10	±0.10
Circular trajectory (mm)	±0.30	±0.10	±0.10
Motorcycle shell trajectory (mm)	±0.40	±0.10	±0.30

The simulation and experimental results of the 7-axis suspended robotic arm (see Tables 8 and 9) indicate that during trajectory tracking for both rectangular and circular paths, using the manifold deformation control method, the maximum tracking errors along the X, Y, and Z axes are all below 0.20 mm and 0.30 mm, respectively. The simulation and experimental data are highly consistent. For trajectory tracking of the motorcycle shell, due to the complexity of the surface shape, the simulation results show maximum tracking errors along the X, Y, and Z axes below 0.20 mm, while the experimental results of the robotic arm show errors below 0.40 mm. Although there is some discrepancy between the two, the results remain very close. This study demonstrates that the manifold deformation control method used in both simulation and experimentation is highly effective, enabling precise control of the 7-axis suspended robotic arm.

Finally, the actual thickness of the spray applied to the motorcycle shell, sprayed by the 7-axis suspended robotic arm (as shown in Figure 16), must meet the manufacturer's requirement of 35–40 μm. To verify compliance with this specification, a thickness testing machine was used to measure the film thickness at four different positions on the motorcycle shell.

(**a**) (**b**)

Figure 16. Measured spray thickness on the motorcycle shell: (**a**) different locations; (**b**) measuring instrument.

The results, displayed in Figure 16, confirm that the measured film thickness falls within the required range. Detailed measurements for each of the four positions are summarized in Table 10, demonstrating consistency in the spray application across different areas of the shell. This consistency highlights the precision and effectiveness of the robotic arm's control system in achieving uniform coating thickness, even on complex and curved surfaces. These findings validate the practical application of the robotic arm in industrial settings where precise and uniform spraying is essential, meeting both quality and performance standards.

Table 10. Measured film thickness at four positions on the motorcycle shell.

Positions	Thickness (μm)
1	36.8
2	37.2
3	36.2
4	36.5

5. Conclusions

This study successfully developed a customized seven-axis suspended robotic arm designed for automated spray-coating production lines. In the design part, factors such as the size of the workspace, dimensions of the workpiece, suspension positions, and spraying actions are analyzed to determine the degrees of freedom and confirm the coordinates of the workspace. This informed decisions regarding the number of axes, lengths of rods, and the configuration of mechanisms, accompanied by 3D modeling of the workspace. Subsequently, servo motors and reducers are selected based on requirements for the weight of the arm, load size, and movement speed. To satisfy the need for flexibility in the workspace, a suspended design is implemented, allowing the robotic arm to be easily stored and moved, resulting in the successful fabrication of the 7-axis suspended robotic

arm. For controlling the robotic arm, three paths are planned: rectangular, circular, and motorcycle shell. The manifold deformation control method is applied in MATLAB R2018A to simulate the robotic arm's trajectory testing for these paths. The results show that the maximum error in the robotic arm's trajectory compared to the planned paths is less than 0.20 mm, indicating that the manifold deformation control method accurately controlled the arm's position. This control method is further implemented on a multi-axis servo control board with an embedded manifold deformation controller to control the physical 7-axis suspended robotic arm in tracing the specified paths. During the arm's movement, the calculated path values in the rectangular coordinate system show maximum errors of less than 0.40 mm when compared to the originally planned values, validating the operational performance of the 7-axis suspended robotic arm's automated spraying system. The multi-axis servo control board with the embedded manifold deformation controller demonstrated excellent control capabilities for the physical arm. Notably, when the arm moved along the path for the motorcycle shell (workpiece), the spray gun installed at the end effector performed the actual spraying operations. The resulting film thickness of the sprayed shell complies with the specified standards, making it suitable for use in the manufacturer's automated spraying production line. Currently, the spray path for the motorcycle shell (workpiece) in this study is planned manually by selecting 3D coordinate points. In the future, visual equipment will be used to detect the motorcycle shell (workpiece) and automatically plan the optimal spray path. Subsequent research will focus on optimizing the control system and other areas to achieve the goal of an intelligent automatic spraying system.

Author Contributions: Conceptualization, C.-C.L. and C.-S.L.; methodology, C.-C.L. and C.-S.L.; software, C.-C.L. and J.-C.L.; validation, C.-C.L., J.-C.L. and C.-S.L.; formal analysis, C.-C.L. and C.-S.L.; investigation, C.-C.L. and J.-C.L.; resources, C.-C.L.; data curation, C.-C.L. and J.-C.L.; writing—original draft preparation, C.-C.L.; writing—review and editing, C.-C.L. and C.-S.L.; visualization, C.-C.L. and J.-C.L.; supervision, C.-C.L.; project administration, C.-C.L.; funding acquisition, C.-C.L. All authors have read and agreed to the published version of the manuscript.

Funding: This research received no external funding.

Data Availability Statement: The data presented in this study are available on request from the corresponding author due to privacy.

Conflicts of Interest: The authors declare no conflict of interest.

References

1. Montironi, M.A.; Castellini, P.; Stroppa, L.; Paone, N. Adaptive autonomous positioning of a robot vision system: Application to quality control on production lines. *Robot. Comput.-Integr. Manuf.* **2014**, *30*, 489–498. [CrossRef]
2. Gil-Vilda, F.; Sune, A.; Yagüe-Fabra, J.A.; Crespo, C.; Serrano, H. Integration of a collaborative robot in a U-shaped production line: A real case study. *Procedia Manuf.* **2017**, *13*, 109–115. [CrossRef]
3. Villani, V.; Pini, F.; Leali, F.; Secchi, C. Survey on human–robot collaboration in industrial settings: Safety, intuitive interfaces and applications. *Mechatronics* **2018**, *55*, 248–266. [CrossRef]
4. Hentout, A.; Aouache, M.; Maoudj, A.; Akli, I. Human–robot interaction in industrial collaborative robotics: A literature review of the decade 2008–2017. *Adv. Robot.* **2019**, *33*, 764–799. [CrossRef]
5. Barosz, P.; Gołda, G.; Kampa, A. Efficiency analysis of manufacturing line with industrial robots and human operators. *Appl. Sci.* **2020**, *10*, 2862. [CrossRef]
6. Chiaverini, S.; Siciliano, B.; Villani, L. A survey of robot interaction control schemes with experimental comparison. *IEEE/ASME Trans. Mechatron.* **1999**, *4*, 273–285. [CrossRef]
7. Xu, D.; Acosta Calderon, C.A.; Gan, J.Q.; Hu, H.; Tan, M. An analysis of the inverse kinematics for a 5-DOF manipulator. *Int. J. Autom. Comput.* **2005**, *2*, 114–124. [CrossRef]
8. Manjaree, S.; Nakra, B.C.; Agarwal, V. Comparative analysis for kinematics of 5-DOF industrial robotic manipulator. *Acta Mech. Autom.* **2015**, *9*, 229–240. [CrossRef]

9. Chen, Z.; Wang, H.; Lu, X.; Pu, Q.; Li, M.; Yan, J. Kinematics analysis and application of 5-DOF manipulator with special joint. In Proceedings of the 2017 Chinese Automation Congress (CAC), Jinan, China, 20–22 October 2017; pp. 7421–7426.
10. Zhong, G.; Peng, B.; Dou, W. Kinematics analysis and trajectory planning of a continuum manipulator. *Int. J. Mech. Sci.* **2022**, *222*, 107206. [CrossRef]
11. Wen, S.; Qin, G.; Zhang, B.; Lam, H.K.; Zhao, Y.; Wang, H. The study of model predictive control algorithm based on the force/position control scheme of the 5-DOF redundant actuation parallel robot. *Robot. Auton. Syst.* **2016**, *79*, 12–25. [CrossRef]
12. Lattanzi, L.; Cristalli, C.; Massa, D.; Boria, S.; Lépine, P.; Pellicciari, M. Geometrical calibration of a 6-axis robotic arm for high accuracy manufacturing task. *Int. J. Adv. Manuf. Technol.* **2020**, *111*, 1813–1829. [CrossRef]
13. Chen, J.I.-Z.; Chang, J.T. Applying a 6-axis mechanical arm combined with computer vision to the research of object recognition in plane inspection. *J. Artif. Intell.* **2020**, *2*, 77–99.
14. Cheng, F.T.; Hour, T.L.; Sun, Y.Y.; Chen, T.H. Study and resolution of singularities for a 6-DOF PUMA manipulator. *IEEE Trans. Syst. Man Cybern. Part B* **1997**, *27*, 332–343. [CrossRef]
15. Kim, D.; Chung, W.; Youm, Y. Singularity analysis of 6-DOF manipulators with the analytical representation of the determinant. In Proceedings of the 1999 IEEE International Conference on Robotics and Automation (Cat. No.99CH36288C), Detroit, MI, USA, 10–15 May 1999; Volume 2, pp. 889–894.
16. Li, S.; Chen, D.; Wang, J. An optimal singularity-free motion planning method for a 6-DOF parallel manipulator. *Ind. Robot. Int. J. Robot. Res. Appl.* **2021**, *48*, 290–299. [CrossRef]
17. Zhang, X.; Fan, B.; Wang, C.; Cheng, X. Analysis of singular configuration of robotic manipulators. *Electronics* **2021**, *10*, 2189. [CrossRef]
18. Jin, Y.; Chen, I.M.; Yang, G. Kinematic design of a 6-DOF parallel manipulator with decoupled translation and rotation. *IEEE Trans. Robot.* **2006**, *22*, 545–551. [CrossRef]
19. Liu, H.; Zhang, T. A new approach to avoid singularities of 6-DOF industrial robots. In Proceedings of the 2010 IEEE International Conference on Mechatronics and Automation, Xi'an, China, 4–7 August 2010; pp. 247–251.
20. Gao, G.; Sun, G.; Na, J.; Guo, Y.; Wu, X. Structural parameter identification for 6-DOF industrial robots. *Mech. Syst. Signal Process.* **2018**, *113*, 145–155. [CrossRef]
21. Djuric, A.; Filipovic, M.; Kevac, L.; Urbanic, J. Singularity Analysis for a 6-DOF Family of Robots. In *Enabling Manufacturing Competitiveness and Economic Sustainability, Proceedings of the 5th International Conference on Changeable, Agile, Reconfigurable and Virtual Production (CARV 2013), Munich, Germany, 6–9 October 2013*; Springer: Berlin/Heidelberg, Germany, 2014; pp. 201–206.
22. Filiposka, M.Z.; Djuric, A.M.; ElMaraghy, W. Complexity analysis for calculating the Jacobian matrix of 6-DOF reconfigurable machines. *Procedia CIRP* **2014**, *17*, 218–223. [CrossRef]
23. Reboucas Filho, P.P.; da Silva, S.P.P.; Praxedes, V.N.; Hemanth, J.; de Albuquerque, V.H.C. Control of singularity trajectory tracking for robotic manipulator by genetic algorithms. *J. Comput. Sci.* **2019**, *30*, 55–64. [CrossRef]
24. Kuhlemann, I.; Jauer, P.; Ernst, F.; Schweikard, A. Robots with seven degrees of freedom: Is the additional DoF worth it? In Proceedings of the 2016 2nd International Conference on Control, Automation and Robotics (ICCAR), Hong Kong, China, 28–30 April 2016; pp. 80–84.
25. Huang, Q.-L.; Wu, J.; Xiong, R. A solution of inverse kinematics for 7-DOF manipulators and its application. In Proceedings of the 10th World Congress on Intelligent Control and Automation, Beijing, China, 6–8 July 2012.
26. Atawnih, A.; Papageorgiou, D.; Doulgeri, Z. Kinematic control of redundant robots with guaranteed joint limit avoidance. *Robot. Auton. Syst.* **2016**, *79*, 122–131. [CrossRef]
27. Asfour, T.; Dillmann, R. Human-like motion of a humanoid robot arm based on a closed-form solution of the inverse kinematics problem. In Proceedings of the 2003 IEEE/RSJ International Conference on Intelligent Robots and Systems (IROS 2003) (Cat. No. 03CH37453), Las Vegas, NV, USA, 27–31 October 2003; Volume 2, pp. 1407–1412.
28. Shimizu, M.; Kakuya, H.; Yoon, W.K.; Kitagaki, K.; Kosuge, K. Analytical inverse kinematic computation for 7-DOF redundant manipulators with joint limits and its application to redundancy resolution. *IEEE Trans. Robot.* **2008**, *24*, 1131–1142. [CrossRef]
29. Yan, L.; Mu, Z.; Xu, W. Analytical inverse kinematics of a class of redundant manipulators based on dual arm-angle parameterization. In Proceedings of the 2014 IEEE International Conference on Systems, Man, and Cybernetics (SMC), San Diego, CA, USA, 5–8 October 2014; pp. 3744–3749.
30. Oh, J.; Bae, H.; Oh, J.H. Analytic inverse kinematics considering the joint constraints and self-collision for redundant 7-DOF manipulator. In Proceedings of the 2017 First IEEE International Conference on Robotic Computing (IRC), Taichung, Taiwan, 10–12 April 2017; pp. 123–128.
31. Chen, Z.; Zeng, Z.; Shu, G.; Chen, Q. Kinematic solution and singularity analysis for 7-DOF redundant manipulators with offsets at the elbow. In Proceedings of the 2018 IEEE Industrial Cyber-Physical Systems (ICPS), St. Petersburg, Russia, 15–18 May 2018; pp. 422–427.
32. Hollerbach, J.M. Optimum kinematic design for a seven degree of freedom manipulator. In *Robotics Research: The Second International Symposium*; MIT Press: Cambridge, MA, USA, 1985; pp. 215–222.

33. Li, S.; Wang, Z.; Zhang, Q.; Han, F. Solving inverse kinematics model for 7-DOF robot arms based on space vector. In Proceedings of the 2018 International Conference on Control and Robots (ICCR), Hong Kong, China, 15–17 September 2018; pp. 1–5.
34. Li, Z.; Brandstötter, M.; Hofbaur, M. Analysis of kinematic singularities for a serial redundant manipulator with 7 DOF. In *Advances in Robot Kinematics 2018*; Springer International Publishing: New York, NY, USA, 2019; pp. 179–186.
35. Chou, W.; Liu, Y. An Analytical Inverse Kinematics Solution with the Avoidance of Joint Limits, Singularity and the Simulation of 7-DOF Anthropomorphic Manipulators. *Trans. FAMENA* **2024**, *48*, 117–132. [CrossRef]
36. Saha, S.K. *Introduction to Robotics*; Tata McGraw-Hill Education: New York, NY, USA, 2014.
37. Wilson, M. *Implementation of Robot Systems: An Introduction to Robotics, Automation, and Successful Systems Integration in Manufacturing*; Butterworth-Heinemann: Oxford, UK, 2014.
38. Kabra, M.P.; Kabra, D.; Somani, G. A review on role of robot in pharmaceutical industry. *Int. J. Inst. Pharm. Life Sci.* **2011**, *1*, 220–237.
39. Olivares-Mendez, M.; Makhdoomi, M.R.; Yalçın, B.C.; Bokal, Z.; Muralidharan, V.; Del Castillo, M.O.; Martínez, C. Zero-G Lab: A multi-purpose facility for emulating space operations. *J. Space Saf. Eng.* **2023**, *10*, 509–521. [CrossRef]
40. Goodno, B.J.; Gere, J. *Statics and Mechanics of Materials*; Cengage Learning: Boston, MA, USA, 2018.
41. Andersson, R.L. Computing the feasible configurations of a 7-DOF arm subject to joint limits. *IEEE Trans. Robot. Autom.* **1993**, *9*, 186–195. [CrossRef]
42. Cui, Z.; Pan, H.; Qian, D.; Peng, Y.; Han, Z. A novel inverse kinematics solution for a 7-DOF humanoid manipulator. In Proceedings of the 2012 IEEE International Conference on Mechatronics and Automation, Chengdu, China, 5–8 August 2012; pp. 2230–2234.
43. Brahmi, B.; Saad, M.; Brahmi, A.; Luna, C.O.; Rahman, M.H. Compliant control for wearable exoskeleton robot based on human inverse kinematics. *Int. J. Adv. Robot. Syst.* **2018**, *15*, 1729881418812133. [CrossRef]
44. Liu, C.S.; Liu, C.C. A manifold deformation design scheme for the controls of nonlinear systems. In Proceedings of theSICE Annual Conference, Taipei, Taiwan, 18–21 August 2010; pp. 3325–3331.
45. Liu, C.S.; Chen, J.S. Robust control using a fixed-manifold design scheme and its applications to robot manipulators. *J. Robot. Syst.* **1998**, *15*, 347–363. [CrossRef]